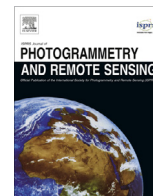




Contents lists available at ScienceDirect

ISPRS Journal of Photogrammetry and Remote Sensing

journal homepage: www.elsevier.com/locate/isprsjprs

Ground subsidence in Tucson, Arizona, monitored by time-series analysis using multi-sensor InSAR datasets from 1993 to 2011



Jin-Woo Kim^{a,*}, Zhong Lu^a, Yuanyuan Jia^b, C.K. Shum^{b,c}

^aRoy M. Huffington Department of Earth Sciences, Southern Methodist University, Dallas, TX, USA

^bDivision of Geodetic Science, School of Earth Sciences, The Ohio State University, Columbus, OH, USA

^cInstitute of Geodesy and Geophysics, Chinese Academy of Sciences, Wuhan, China

ARTICLE INFO

Article history:

Received 13 March 2014

Received in revised form 26 January 2015

Accepted 23 March 2015

Available online 23 April 2015

Keywords:

InSAR

SBAS

Groundwater extraction

Tucson

Aquifer-system compaction

Ground subsidence

ABSTRACT

The groundwater in Tucson, Arizona, is a major source for water supply to human residential areas and agricultural use, and the groundwater extraction causes ground deformation responding to aquifer-system compaction. Using multi-temporal C-band and L-band SAR images from ERS/ENVISAT and ALOS PALSAR satellites, we mapped the ground displacement in Tucson. The InSAR-derived ground displacement based on small baseline subset technique (SBAS) is compared to compaction from extensometers, land subsidence from GPS survey, and groundwater elevation at wells. Tucson is characterized by slow and relatively small subsidence over areas with upper stratigraphic till early 2000s when the groundwater had been extremely depleted and by uplifts in areas where the water level has been recently recovered into the slight increase of water table because of recharge into the aquifer. Our multi-sensor SBAS InSAR-derived vertical displacements enabled to monitor the temporal variability in the spatial extent and magnitude of the ground deformation, suggesting that recent ground subsidence is slowing down and the ground motion in places is stable. Our results can provide scientific basis for sound management of ground water pumping and recharge over the study area.

© 2015 International Society for Photogrammetry and Remote Sensing, Inc. (ISPRS). Published by Elsevier B.V. All rights reserved.

1. Introduction

The groundwater is a major source for supplying drinking water to residents in arid lands, irrigating plants for agriculture, and flowing into lakes or rivers. The rain water, snowmelt, and inflow from upper watershed leads into the recharge of groundwater, and the discharge is made by natural flow and human demands for industrial, municipal, and agricultural purposes. Natural condition is balancing between recharge and discharge, but the balance has been threatened by extreme consumption of groundwater for developing arid areas of Phoenix and Nevada in the United States, Libya, and India. The groundwater depletion caused the disappearance of a crucial water resource as well as the aquifer-system compaction and ground subsidence. More than 80 percent of the identified subsidence in the United States is caused by human activities on subsurface water (Galloway et al., 2000). To conserve the groundwater and circumvent more rapid

consumption from the subsurface, the elaborate resource management and intensive governmental efforts are required.

In Tucson, Arizona, the groundwater has been a critical resource for urban and rural communities, and the rapid urbanization and growing population has been heavily dependent on groundwater because of the lack of surface water. The excessive consumption of groundwater led to the decrease of water table as much as 14 m between 1989 and 2005, and the declined water level before 1989 was much bigger than this number (Carruth et al., 2007). The groundwater pumping in excess of natural recharge was the major cause of aquifer-system compaction and associated land subsidence in Tucson area (Pool and Anderson, 2008). Since the Arizona's 1980 Groundwater Management Act, the temporal variations of groundwater table, soil compaction, and land subsidence have been monitored by gauges in wells, borehole extensometers, and annual GPS survey at multiple stations (Carruth et al., 2007; Pool and Anderson, 2008). These methods provide a good precision of measurement on subsurface condition, but each has limitation in detecting land-surface motion over large areas associated with groundwater depletion. For example, the water level at wells is not highly correlated with surface deformation in many cases, and the extensometers cannot measure the compaction occurring

* Corresponding author at: Roy M. Huffington Department of Earth Sciences, Southern Methodist University, 3225 Daniel Avenue, Room 210, Dallas, TX 75205, USA. Tel.: +1 214 768 2750; fax: +1 214 768 2701.

E-mail addresses: jinwook@mail.smu.edu, chowoon97@gmail.com (J.-W. Kim).

Table 1
SAR images used for ERS, ENVISAT, and ALOS SBAS processing.

Mission	Date	Path	Direction	Incidence Angle (°)	Mission	Date	Path	Direction	Incidence Angle (°)
ERS	1993/06/22	456	Descending	23.2711	ENVISAT	2006/06/23	456	Descending	22.7884
ERS	1993/11/09	456	Descending	23.2711	ENVISAT	2006/11/10	456	Descending	22.7884
ERS	1996/01/11	456	Descending	23.2711	ENVISAT	2007/02/23	456	Descending	22.7884
ERS	1996/01/12	456	Descending	23.2711	ENVISAT	2007/06/08	456	Descending	22.7884
ERS	1996/04/25	456	Descending	23.2711	ENVISAT	2007/08/17	456	Descending	22.7884
ERS	1996/04/26	456	Descending	23.2711	ENVISAT	2007/10/26	456	Descending	22.7884
ERS	1996/11/22	456	Descending	23.2711	ENVISAT	2008/02/08	456	Descending	22.7884
ERS	1997/01/31	456	Descending	23.2711	ENVISAT	2008/05/23	456	Descending	22.7884
ERS	1997/03/07	456	Descending	23.2711	ENVISAT	2008/09/05	456	Descending	22.7884
ERS	1997/08/29	456	Descending	23.2711	ENVISAT	2009/04/03	456	Descending	22.7884
ERS	1999/10/08	456	Descending	23.2711	ENVISAT	2009/07/17	456	Descending	22.7884
ERS	1999/11/12	456	Descending	23.2711	ENVISAT	2009/09/25	456	Descending	22.7884
ERS	2000/01/21	456	Descending	23.2711	ENVISAT	2010/02/12	456	Descending	22.7884
ERS	2000/07/14	456	Descending	23.2711	ENVISAT	2010/04/23	456	Descending	22.7884
ERS	2000/08/18	456	Descending	23.2711	ENVISAT	2010/05/28	456	Descending	22.7884
ERS	2000/09/22	456	Descending	23.2711	ENVISAT	2010/09/10	456	Descending	22.7884
ERS	2002/04/05	456	Descending	23.2711	ALOS	2009/10/17	203	Ascending	38.7249
ENVISAT	2004/01/30	456	Descending	22.7884	ALOS	2009/12/02	203	Ascending	38.7249
ENVISAT	2004/04/09	456	Descending	22.7884	ALOS	2010/01/17	203	Ascending	38.7249
ENVISAT	2004/05/14	456	Descending	22.7884	ALOS	2010/04/19	203	Ascending	38.7249
ENVISAT	2004/07/23	456	Descending	22.7884	ALOS	2010/06/04	203	Ascending	38.7249
ENVISAT	2004/11/05	456	Descending	22.7884	ALOS	2010/12/05	203	Ascending	38.7249
ENVISAT	2004/12/10	456	Descending	22.7884	ALOS	2011/01/20	203	Ascending	38.7249
ENVISAT	2006/03/10	456	Descending	22.7884	ALOS	2011/03/07	203	Ascending	38.7249
ENVISAT	2006/04/14	456	Descending	22.7884					

below the anchor depth of the devices. The annual GPS survey in sparse stations, which is labor-intensive, does not measure the surface displacement with high accuracy like continuous GPS. In contrast, the spatially detailed images of ground displacements generated from SAR interferometry (InSAR) can help to monitor the ground subsidence in Tucson.

The InSAR is an invaluable tool for measuring displacements over a large area with high accuracy of sub-centimeter and high spatial resolution of 30 m after spatial averaging and geocoding. The InSAR processing for detecting displacements after removing topographic and orbital error phases and reducing as much atmospheric artifact as possible is particularly called the differential InSAR (DInSAR). The DInSAR has been used for detecting horizontal and vertical displacements caused by catastrophic natural disasters of earthquakes and volcanoes, anthropologic deformation caused by mining and oil/gas extraction, and deformation induced by melting of permafrost (Hanssen, 2001; Tong et al., 2010; Lu, 2007; Samsonov et al., 2011).

In particular, the DInSAR was used for measuring the surface displacements related to aquifer system compaction and uplift accompanying groundwater discharge and recharge (Lu and Danskin, 2001; Galloway and Hoffmann, 2007). Several researchers (Galloway et al., 1998; Hoffmann and Zebker, 2003) mapped aquifer-system compaction and subsidence in the Antelope Valley, California, by integrating DInSAR, GPS, and extensometers, and successfully estimated the groundwater flow, storage change, and compaction over large areas. The water decline and clay thickness map in Las Vegas Valley was analyzed with subsidence map based on DInSAR, GPS, and leveling (Amelung et al., 1999; Bell et al., 2002) and inelastic and elastic deformation caused by seasonal variation was detected by DInSAR time-series analysis. Schmidt and Burgmann (2003) used the DInSAR for measuring surface subsidence by groundwater extraction in Santa Clara Valley, California and found the Silver Creek Fault to disrupt the groundwater flow and cause steep displacement gradients. The recent advance in the DInSAR technology can improve the accuracy of surface deformation measurements. The small baseline subset (SBAS) algorithm exploiting multi differential interferograms of small baselines could be used to enhance the understanding of the underlying

deformation process in the groundwater-withdrawn region with dense temporal interval (Berardino et al., 2002). The advantage of SBAS technique is that it could minimize the atmospheric phase in InSAR pairs, capture the pattern of deformation in time and space, and estimate non-linear time series of deformation during a long time span by analyzing DInSAR pairs with short perpendicular baselines (Berardino et al., 2002; Lanari et al., 2004; Samsonov et al., 2011).

In this paper, the SBAS InSAR technology was applied for detecting ground subsidence in Tucson, caused by groundwater depletion. Using sufficient SAR data archive from early 1990s to 2011, the spatial extent and magnitude of surface deformation in Tucson has been estimated. Our study utilized ERS-1/2, ENVISAT, and ALOS PALSAR, and the results of multi-sensor SBAS InSAR processing are analyzed in spatio-temporal scale with supplementary data from gauges, extensometers, and GPS survey.

2. Methodology

Standard DInSAR processing with small perpendicular baselines is required before performing SBAS InSAR processing. The N interferograms are generated from M SAR images, which are coregistered on a common master image, by multiplying master complex image with a conjugate of slave complex SAR data. To avoid spatial decorrelation, a small orbital separation should be selected for further time-series analysis. Moreover, the threshold of temporal baselines based on radar frequency and coherence should be considered to prevent temporal decorrelation. The interferometric phase of each interferogram is composed of a phase component caused by deformation, topography, orbital error, atmosphere, and random noise term, respectively. The phase components but deformation are reduced by using digital elevation model (DEM), least-square fitted 2nd order polynomial, and noise-suppressing filters. Because topography provided by DEM sources has relative error terms and atmospheric phase is not easy to be removed from a single InSAR pair, the deformation phase cannot be reliably obtained. If there is no phase unwrapping error, the observed interferometric phase ϕ_{ifgs}^k of k th differential

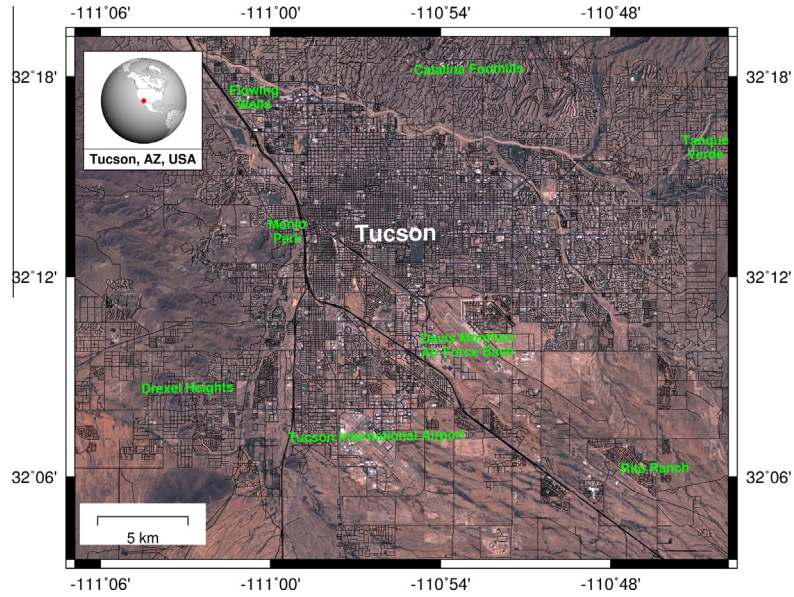


Fig. 1. Tucson metropolitan area located in Pima county, Arizona.

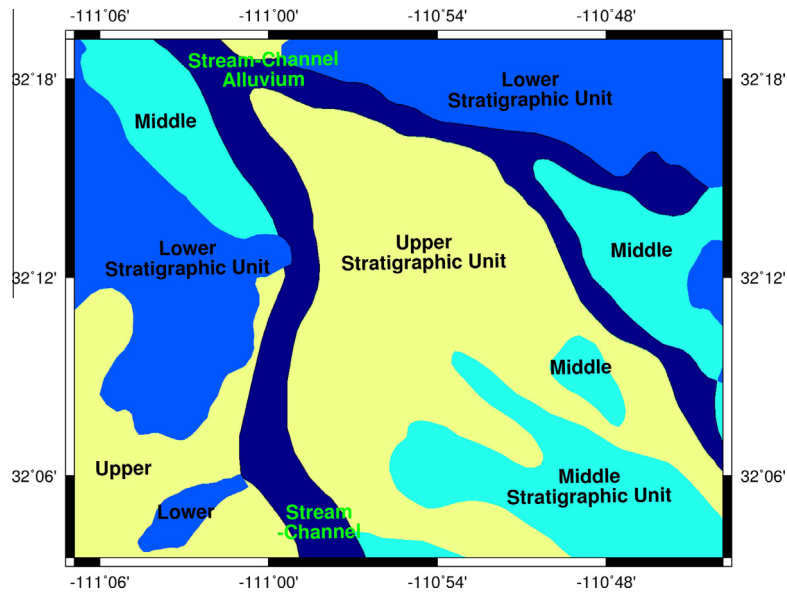


Fig. 2. Generalized geological map in Tucson metropolitan area. The geological composition consists of upper, middle, and lower stratigraphic units. The area with upper stratigraphic unit is subject to ground deformation.

interferogram consists of deformation ϕ_{def}^k , topographic ϕ_{topo}^k , atmospheric ϕ_{atm}^k , and noise ϕ_{noise}^k ,

$$\phi_{ifgs}^k = \phi_{def}^k + \phi_{topo}^k + \phi_{atm}^k + \phi_{noise}^k \quad (1)$$

In Eq. (1), both topographic phase and atmospheric phase terms are related to errors and residuals in DInSAR processing. The residual topographic phase term is estimated as (Berardino et al., 2002; Samsonov, 2010),

$$\phi_{topo}^k = \frac{B_{\perp} \cdot \Delta z}{R \cdot \sin \theta} \quad (2)$$

where R is the line-of-sight distance between satellites and targets, θ is incidence angles, B_{\perp} is perpendicular baselines, and Δz is topographic error term. The atmospheric phase can be classified into turbulent mixing and vertical stratification

contributions (Hanssen, 2001). The turbulent contributions are considered as a random phase both in space and time while the vertical stratification contribution is correlated with elevation (López-Quiroz et al., 2009). Removing the effect of vertical stratification is a relatively easy step by using a linear correlation between interferometric phase from each interferogram and elevation from DEM, but the turbulent contribution, assumed as random, can be reduced by computing a least square solution from many interferograms acquired under favorable conditions less influenced by spatial and temporal decorrelation (Samsonov et al., 2013). The key feature of SBAS InSAR is that it can reduce the random atmospheric phase from many InSAR pairs as well as estimating topographic error terms related to the perpendicular baseline. Additionally, ionospheric effects can induce the azimuthal image and Doppler Centroid distortion on low frequency (L-band) radar system (Franz et al., 2006), but

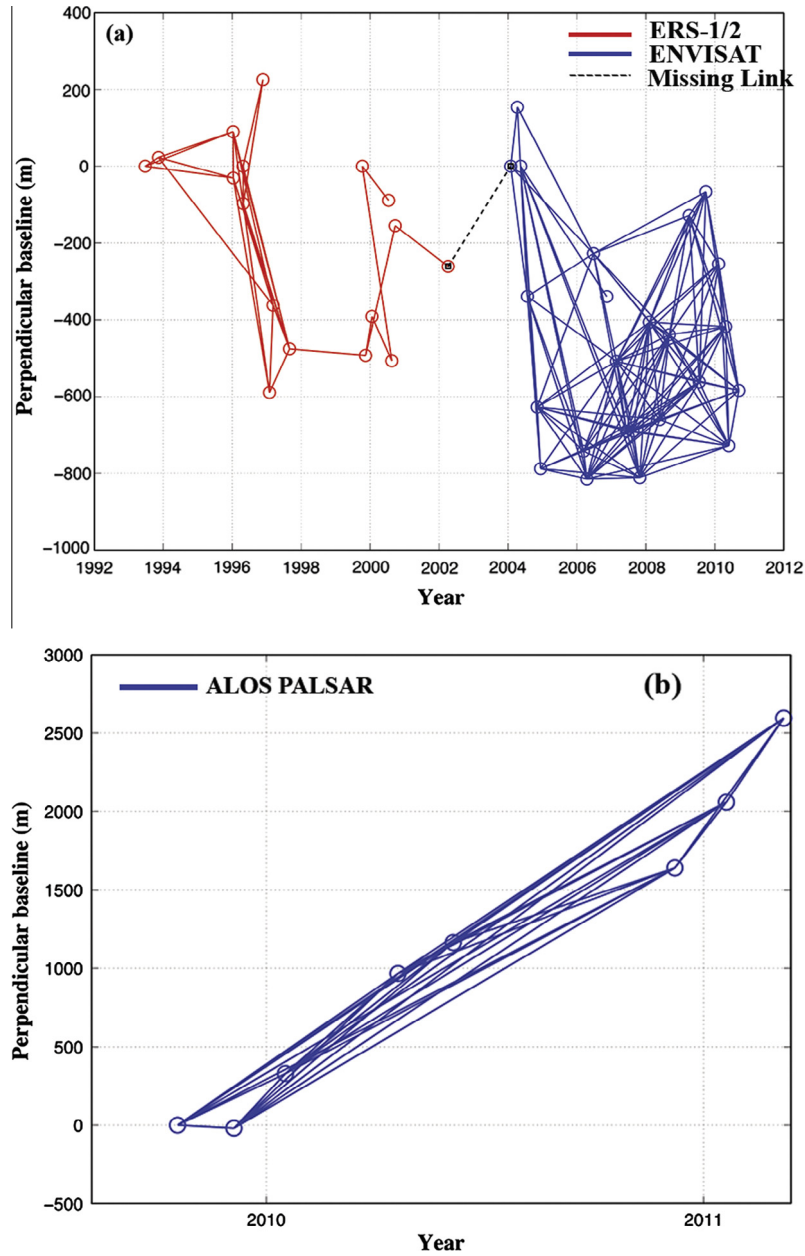


Fig. 3. Diagram of perpendicular and temporal baseline of InSAR pairs ((a) ERS and ENVISAT InSAR pairs; red circles and lines are 29 ERS pairs, and blue circles and lines are 134 ENVISAT pairs. And, dashed black line represents simulated temporary InSAR pair to fill up data gap. (b) ALOS PALSAR InSAR pairs). (For interpretation of the references to colour in this figure legend, the reader is referred to the web version of this article.)

the artifacts due to ionosphere were negligible in our used L-band SAR images.

To integrate the InSAR pairs from multi-sensor, additional process is needed to correct the effect of the different wavelengths. As proposed by a previous study (Pepe et al., 2005), ERS and ENVISAT SAR sensors have different center frequency (5.30 GHz for ERS-1/2 and 5.33 GHz for ENVISAT ASAR) and it is difficult to generate interferogram from ERS/ENVISAR pairs. Instead, the ENVISAT InSAR pairs can be integrated into SBAS algorithm, by multiplying the correction term ($\lambda_{ENVISAT}/\lambda_{ERS}$, $\lambda_{ERS} = 5.656$ cm and $\lambda_{ENVISAT} = 5.624$ cm) with unwrapped interferometric phases. If the track of ENVISAT and ERS is identical, the incidence angle of ERS and ENVISAT is similar in most cases (Table 1).

The fundamental equation for SBAS can be expressed as the following form,

$$Bv = \Phi_{ifgs} \quad (3)$$

where B matrix has dimensions of N by $M - 1$ (N and M are the numbers of interferograms and SAR images, respectively), Φ_{ifgs} ($N \times 1$) is a vector of observed interferometric phase ϕ_{ifgs}^k , and v vector consists of $M - 1$ mean velocities between time-adjacent acquisitions to be calculated. The v vector is unknown as,

$$v^T = \left(v_1 = \frac{\phi_1^{inc}}{t_2 - t_1} \cdots v_k = \frac{\phi_k^{inc}}{t_{k+1} - t_k} \cdots v_{M-1} = \frac{\phi_{M-1}^{inc}}{t_M - t_{M-1}} \right) \quad (4)$$

where ϕ_k^{inc} is an incremental phase from t_k (acquisition date of k th SAR data) to t_{k+1} (acquisition date of $k + 1$ th SAR data). In B matrix, if a k th interferogram spans the time represented by the column n , then the b_n^k term is equal to the time interval between the consequent images, otherwise zero (Berardino et al., 2002; Samsonov, 2010). In order to correct the topographic error, a perpendicular baseline of each interferogram should be attached to the right side

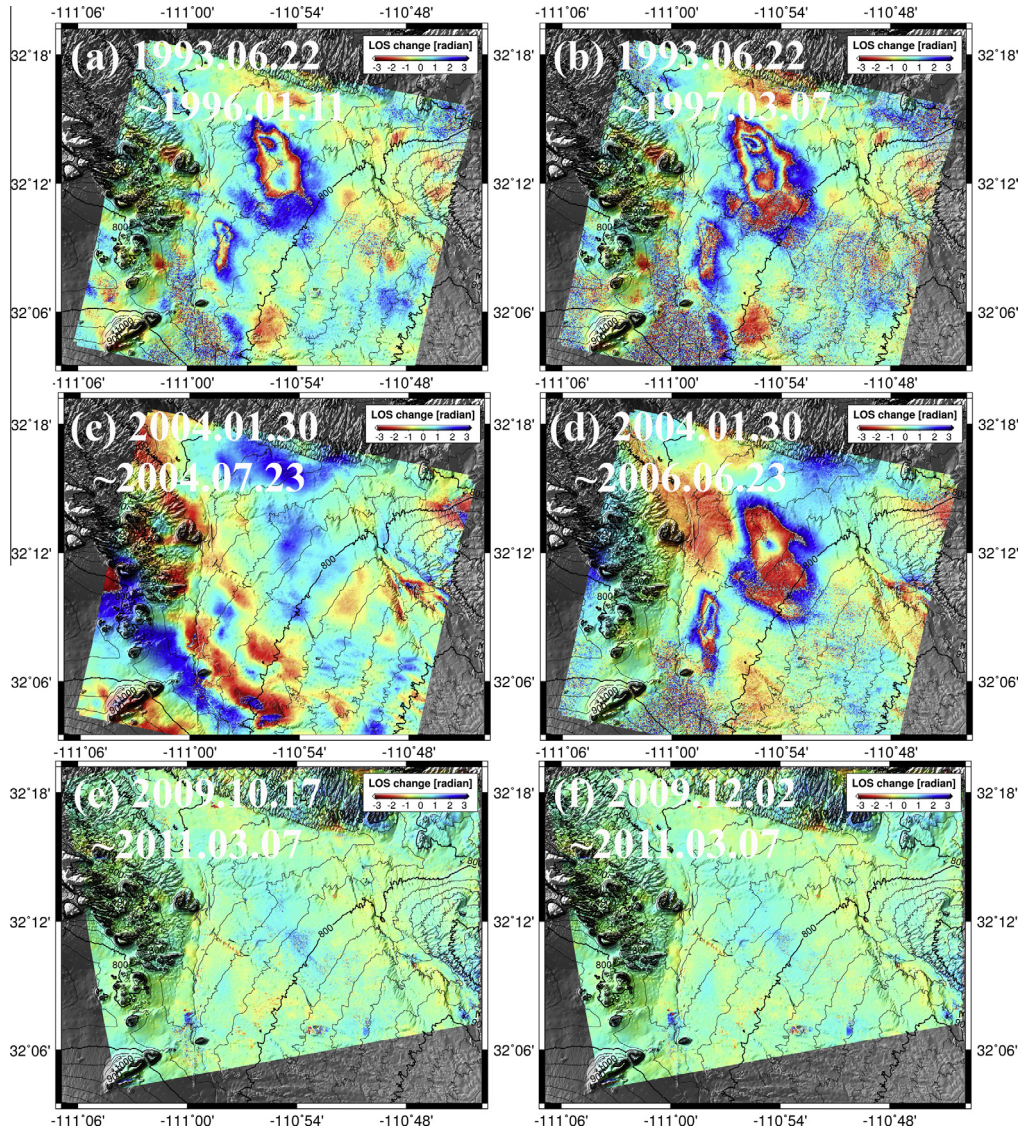


Fig. 4. ERS-1/2 differential interferogram ((a) 1993.06.22–1996.01.11, (b) 1993.06.22–1997.03.07), ENVISAT differential interferogram ((c) 2004.01.30–2004.07.23, (d) 2004.01.30–2006.06.23), ALOS PALSAR differential interferogram ((e) 2009.10.17–2011.03.07, (f) 2009.12.02–2011.03.07).

of the B matrix. Additionally, in low coherence areas, which do not have consistent scattering between acquisition dates, the interferometric phase is set to zero, and the phase value should be excluded for SBAS analysis.

For example, if we assume that four SAR images are acquired at time of t_1, \dots, t_4 five interferograms are generated from intervals $t_2 - t_1, t_3 - t_1, t_3 - t_2, t_4 - t_2, t_4 - t_3$, and the interferometric phase at a pixel of a particular pair (here, InSAR pair between $t_2 - t_3$) is zero due to low coherence, which could be improperly estimated as non-deformation, the SBAS equation can be formulated as ($\Phi_{ifgs} = TBv = \tilde{B}v$ (5)),

$$\begin{pmatrix} \phi_{ifgs}^{1-2} \\ \phi_{ifgs}^{1-3} \\ \phi_{ifgs}^{2-3} \\ \phi_{ifgs}^{2-4} \\ \phi_{ifgs}^{3-4} \end{pmatrix} = \begin{pmatrix} 1 & 0 & 0 & 0 & 0 \\ 0 & 1 & 0 & 0 & 0 \\ 0 & 0 & 0 & 0 & 0 \\ 0 & 0 & 0 & 1 & 0 \\ 0 & 0 & 0 & 0 & 1 \end{pmatrix} \begin{pmatrix} t_2 - t_1 & 0 & 0 & B_{\perp}^{1-2} \\ t_2 - t_1 & t_3 - t_2 & 0 & B_{\perp}^{1-3} \\ 0 & t_3 - t_2 & 0 & B_{\perp}^{2-3} \\ 0 & t_3 - t_2 & t_4 - t_3 & B_{\perp}^{2-4} \\ 0 & 0 & t_4 - t_3 & B_{\perp}^{3-4} \end{pmatrix} \begin{pmatrix} v_1 \\ v_2 \\ v_3 \\ \frac{\Delta z}{R \sin \theta} \end{pmatrix} \quad (5)$$

If pixels of all interferograms have high coherence and their phase unwrapping is properly performed, T matrix will be same as I ($N \times N$) identity matrix. When interferometric phase of k th interferogram is set to zero due to low coherence, $k \times k$ diagonal term of T matrix will be zero. Due to the introduction of T transformation matrix, changing the size of design matrix B is not needed for pixels of all interferograms. Another problem of \tilde{B} ($N \times M$) matrix is a rank deficiency, because critical links of InSAR networks are often missing (i.e. unlinked InSAR pairs in Fig. 3) due to low coherence of many pairs. In addition, the images might be divided to separate networks due to the baseline configuration. The combination of all available interferograms is based on a minimum norm criterion of the velocity deformation (Berardino et al., 2002). The SVD (Singular Value Decomposition) inversion of \tilde{B} matrix enables to solve Eq. (5) and obtain the unknown v vector, but the incremental phase delay of v vector is set to zero by SVD, which biases the subsidence temporal behavior and subsidence rate (López-Quiroz et al., 2009). The solution for the problem is using Tikhonov regularization (Tikhonov and Arsenin, 1977) or low-pass filtering in the time domain

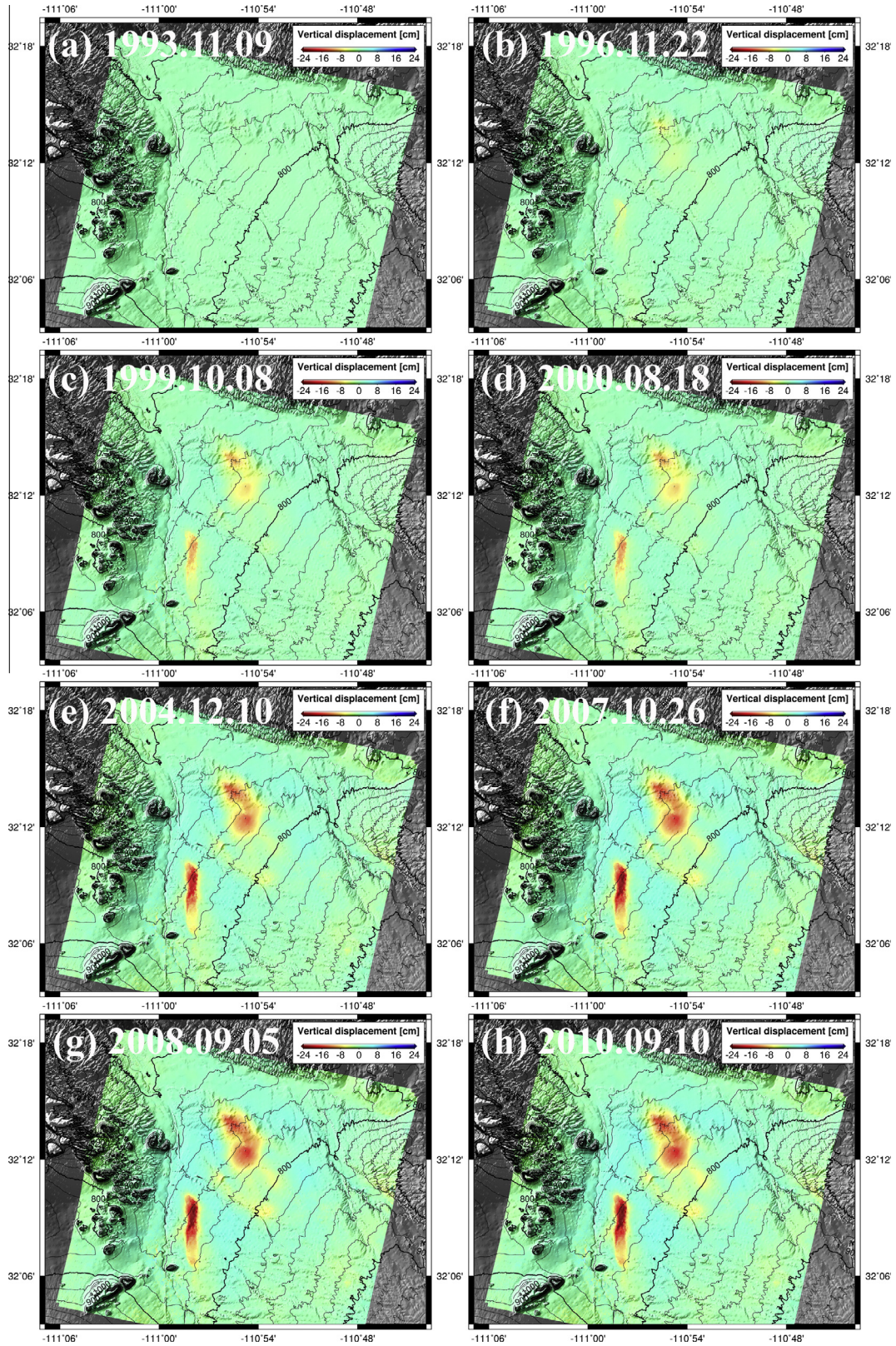


Fig. 5. Time-series of (accumulated) vertical deformations from ERS/ENVISAT SBAS InSAR processing of (a) 1993.11.09, (b) 1996.11.22, (c) 1999.10.08, (d) 2000.08.18, (e) 2004.12.10, (f) 2007.10.26, (g) 2008.09.05, and (h) 2010.09.10.

(Samsonov and d'Oreye, 2012). Another solution is considering the quadratic behavior of the incremental phase delay and adding constraints to design matrix \tilde{B} . The solution supposes that deformation

increases or decreases with second order polynomials in time. Additionally, applying Gaussian filter in time to estimated incremental phase smoothes deformation with avoiding the effect of

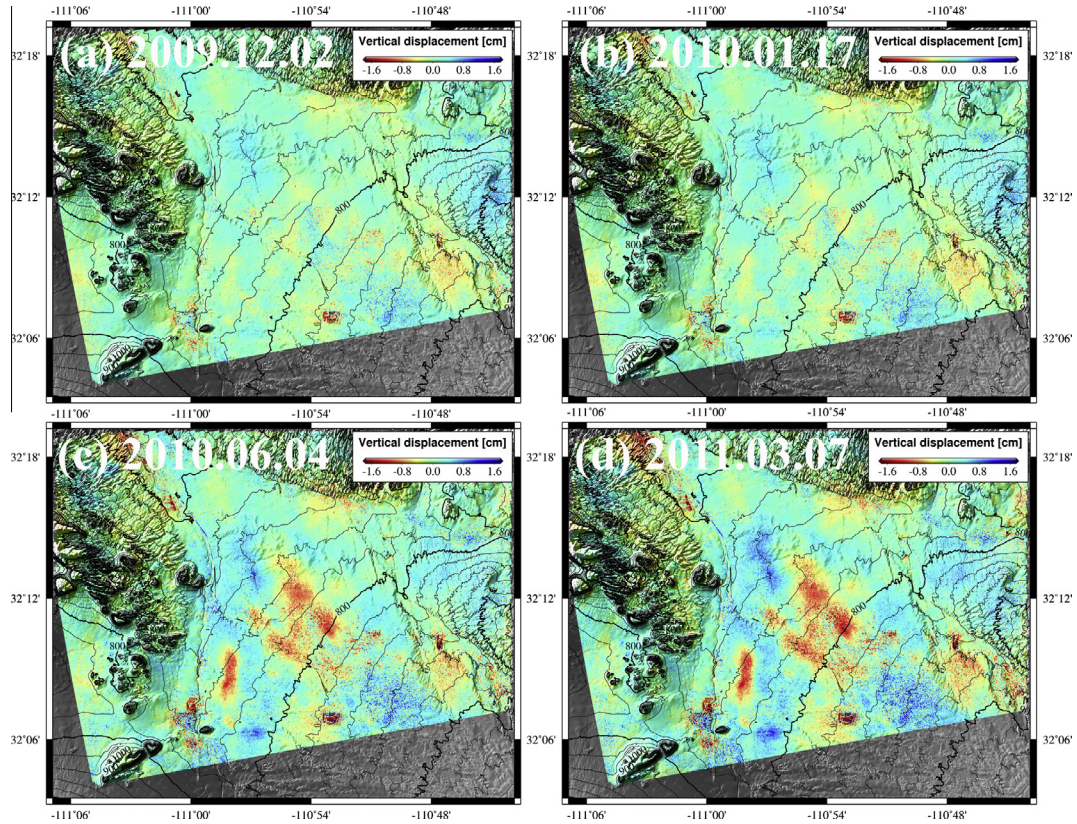


Fig. 6. Time-series of (accumulated) vertical deformations from ALOS SBAS InSAR processing of (a) 2009.12.02, (b) 2010.01.17, (c) 2010.06.04, and (d) 2011.03.07.

rank-deficiency and residual atmospheric error. We added the following constrain to the inversion as proposed by previous study (López-Quiroz et al., 2009),

$$\sum_{k=1}^m \phi_k^{inc} = a(t_m - t_1) + b(t_m - t_1)^2 + c \quad (6)$$

where a, b, c are constants describing the quadratic behavior of incremental phase terms of v vector at time of m . After this constraint is added to Eq. (5), the matrix system becomes $\Phi_{ifgs}^c = B^c v^c$

$$\begin{pmatrix} \phi_{ifgs}^1 \\ \vdots \\ \phi_{ifgs}^N \\ 0 \\ \vdots \\ 0 \end{pmatrix} = \gamma \cdot \begin{pmatrix} t_2 - t_1 & 0 & 0 & \cdots & 0 & 0 & -(t_2 - t_1) & -(t_2 - t_1)^2 & -1 \\ t_2 - t_1 & t_3 - t_2 & \ddots & 0 & \vdots & 0 & -(t_2 - t_1) & -(t_2 - t_1)^2 & -1 \\ t_2 - t_1 & t_3 - t_2 & t_4 - t_3 & \vdots & 0 & \vdots & \vdots & \vdots & \vdots \\ \vdots & \vdots & \ddots & 0 & \vdots & 0 & \vdots & \vdots & -1 \\ t_2 - t_1 & t_3 - t_2 & \cdots & t_{M-1} - t_{M-2} & 0 & \vdots & \vdots & \vdots & \vdots \\ \cdots & \cdots & \cdots & t_M - t_{M-1} & 0 & 0 & -(t_M - t_1) & -(t_M - t_1)^2 & -1 \end{pmatrix} \begin{pmatrix} 0 & 0 & 0 \\ \vdots & \vdots & \vdots \\ 0 & 0 & 0 \\ \vdots & \vdots & \vdots \end{pmatrix} \begin{pmatrix} v_1 \\ \vdots \\ v_{M-1} \\ \frac{\Delta z}{R \cdot \sin \theta} \\ a \\ b \\ c \end{pmatrix} \quad (7)$$

where the weight γ is a scaling factor for the additional matrix of B^c $((N + M - 1) \times (M + 3))$, and the factor should be small enough so as not to affect the inversion of the major design matrix \tilde{B} . The

inversion of $B_c^T B_c$ calculates the incremental phase delay included in v vector and its integration results in the cumulative deformation phase at particular time.

3. Study area and data processing

3.1. Characteristics of study region

Our study region is Tucson city in Arizona of southwest USA (Fig. 1). The city's elevation ranges from 600 to 1300 m, and most

residential areas in downtown are located between 800 m and 900 m at a relatively flat area contrary to mountains in the west (Tucson mountains) and north (Santa Catalina mountains). The

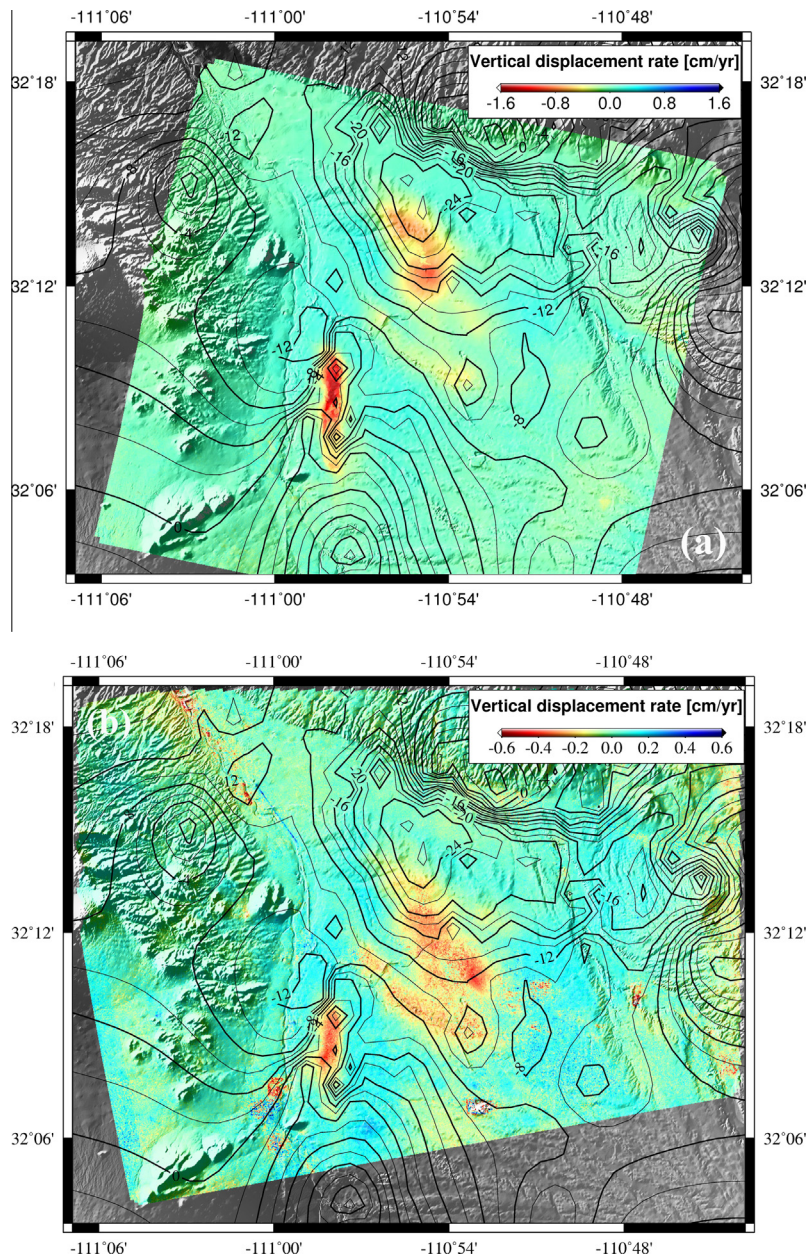


Fig. 7. Linear vertical deformation rate (cm/yr) estimated from (a) ERS/ENVISAT and (b) ALOS SBAS processing. The red-colored region represents ground subsidence due to groundwater extraction. The contour means the iso-lines of groundwater level changes measured in wells. (For interpretation of the references to colour in this figure legend, the reader is referred to the web version of this article.)

Santa Cruz River, which flew along the west side of the Tucson, was a perennial river, but now a dry river bed for most of the year except flooding by seasonal rains. Since the Santa Cruz River became dry and the surface water had been gradually vanished, the city has been dependent on the pumping of groundwater for residential use and agricultural irrigation. Consequently, the water level measured in wells has been dramatically dropped as much as 30 m since 1900s. The land subsidence and earth fissure occurred in Tucson and southern Arizona and damaged the roads and civilian properties, but the phenomenon is depending on the geological condition. The aquifer-compaction and land subsidence are associated with many parameters including soil composition, clay thickness, and soil consolidation. The groundwater withdrawal in dry lands does not necessarily mean ground subsidence, because regions with over-consolidated and incompressible soil, or relatively thin aggregate clay thickness are less sensitive to the

variation of water table in aquifer. Furthermore, in areas with thick aquitards, the subsidence is often delayed after water table is decreased (Galloway and Hoffmann, 2007). The geological composition in Tucson can be grouped into three stratigraphic units (lower, middle, and upper) and stream-channel alluvium (Fig. 2). The lower stratigraphic unit consists of conglomerate, sandstone, mudstone, and gypsiferous mudstone. The middle stratigraphic unit consists of clayey silt, mudstone, and gravel conglomerate. The upper stratigraphic unit consists of gravel, clayey silt, and thin surficial alluvial deposits (Carruth et al., 2007). Among those stratigraphic units, the upper stratigraphic unit is more subject to land subsidence by groundwater extraction and, therefore, the Tucson regions with upper stratigraphic unit have been more exposed to land subsidence. To recover the groundwater storage and stop water level declines during the last several decades, the Central Arizona Project pumped significant artificial

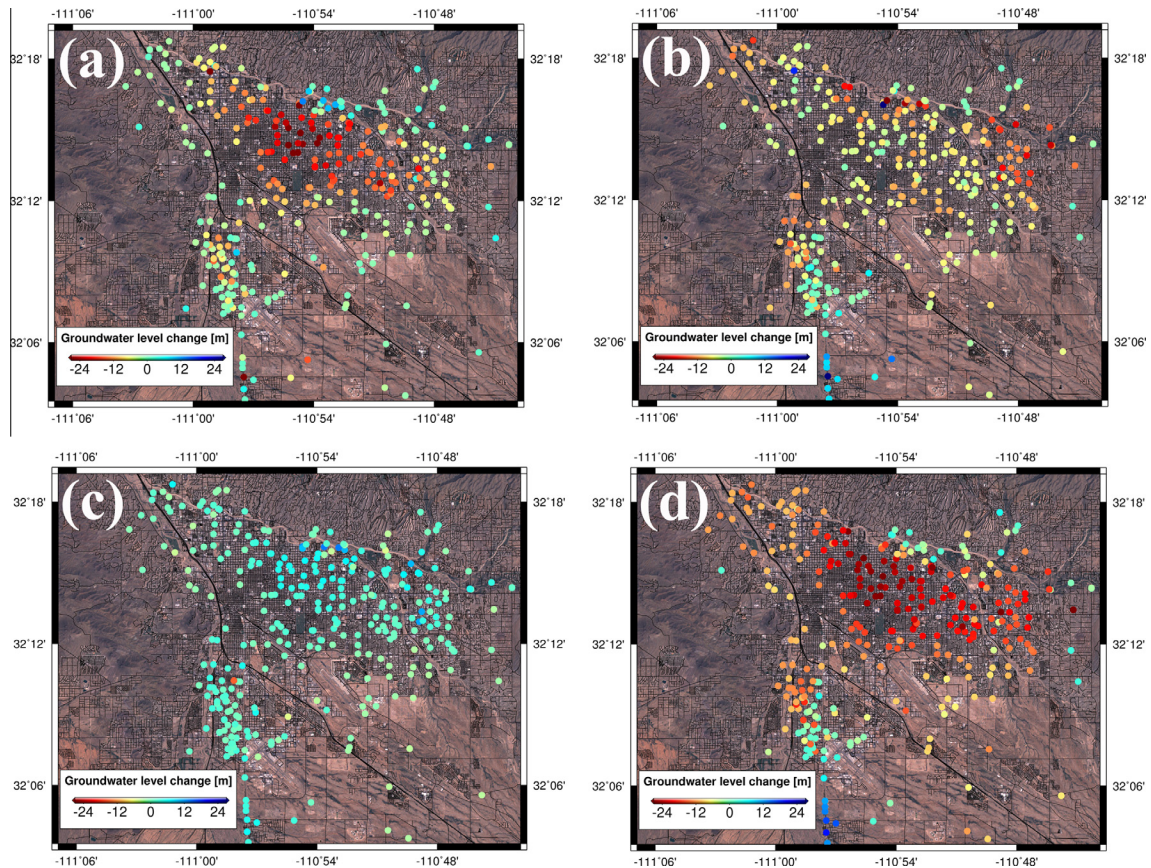


Fig. 8. 10-year interval groundwater level changes measured at wells of (a) 1980s–1990s, (b) 1990s–2000s, and (c) 2000s–2010s, and 30-year water level changes of (d) 1980s–2010s. The red and blue colored dots mean the increase and decrease of water level at wells. (For interpretation of the references to colour in this figure legend, the reader is referred to the web version of this article.)

recharge into the aquifer. As a result, the recent groundwater withdrawal has been decreased, and the water level in many wells indicates the increase of water table (Pool, 2005; Carruth et al., 2007).

3.2. SBAS data processing

For this study, 17 ERS-1/2, 24 ENVISAT ASAR, and 8 ALOS PALSAR images (listed in Table 1), covering the Tucson metropolitan area (Fig. 1), were utilized. ERS-1/2 images including two ERS-1/2 tandem pairs of January, 11, 1996–January, 12, 1996 and April, 25, 1996–April, 26, 1996 were acquired from 1993 to 2002. ENVISAT ASAR images are obtained between 2004 and 2010. Both ERS and ENVISAT ASAR images are from the same descending track of 456 (Table 1), meaning a similar radar geometry, but ERS/ENVISAT InSAR pair cannot be generated due to the difference in center frequency. There is no temporal overlap of ERS and ENVISAT SAR data, causing a data gap between 2002 and 2004. The ALOS PALSAR images were acquired from ascending track, and the ALOS images covers a relatively short time period from late 2009 to 2011 in contrast to C-band sensors.

For SBAS processing, ERS and ENVISAT InSAR pairs with perpendicular baselines smaller than 500 m are generated. Furthermore, InSAR pairs with a good coherence should be selected for reliable DInSAR processing including phase unwrapping (Fig. 3(a) and (b)). 28 ALOS InSAR pairs (Fig. 3(b)) are also created from all 8 SAR images, because L-band InSAR pairs in Tucson are less influenced by temporal and spatial decorrelation related to a large perpendicular baseline and a long time interval (Sandwell et al., 2008).

1-arcsec national elevation dataset (NED) was used to remove topographic contributions in DInSAR processing of ERS, ENVISAT and ALOS pairs. The precise orbit information of ERS and ENVISAT is provided by Delft institute for earth-oriented space research (DEOS). However, several InSAR pairs of ERS, ENVISAT, and ALOS are deteriorated by orbital error fringes, which are then removed by 2nd order polynomial estimation in range and azimuth direction. From the figures (Fig. 4) of ERS, ENVISAT, and ALOS differential interferograms, one can recognize that there are only few phase variations in ALOS InSAR images (Fig. 4(e) and (f)), as the L-band sensor (wavelength of ~ 24 cm) is less sensitive to slow-developing deformation by groundwater extraction in Tucson (i.e. 2.2 (C-band) and 0.53 (L-band) radian change according to 1 cm line-of-sight change) (Luo et al., 2014). Also, it is recognizable that C-band interferograms of Fig. 4(a–d) shows obvious signatures of ground subsidence in downtown of Tucson, but other generated interferograms, not included in Fig. 4, are deteriorated by atmospheric artifacts, particularly turbulent contributions that do not correlate in time. In contrast, the effects of vertical stratification were negligible due to the flat terrain of our study area and their correction was not applied. For example, Fig. 4(c) spans a short period, but many areas in the interferogram contain atmospheric artifacts. Phase unwrapping after smoothing interferograms was applied by minimum cost flow (MCF) algorithm.

One problem in integrating ERS and ENVISAT to SBAS algorithm in our dataset is a data gap between the two groups of InSAR pairs (Fig. 3(a)), and the gap causes a rank deficiency in SBAS processing owing to missing a critical link. To solve the problem, the linear deformation rate is estimated from each ERS and ENVISAT SBAS

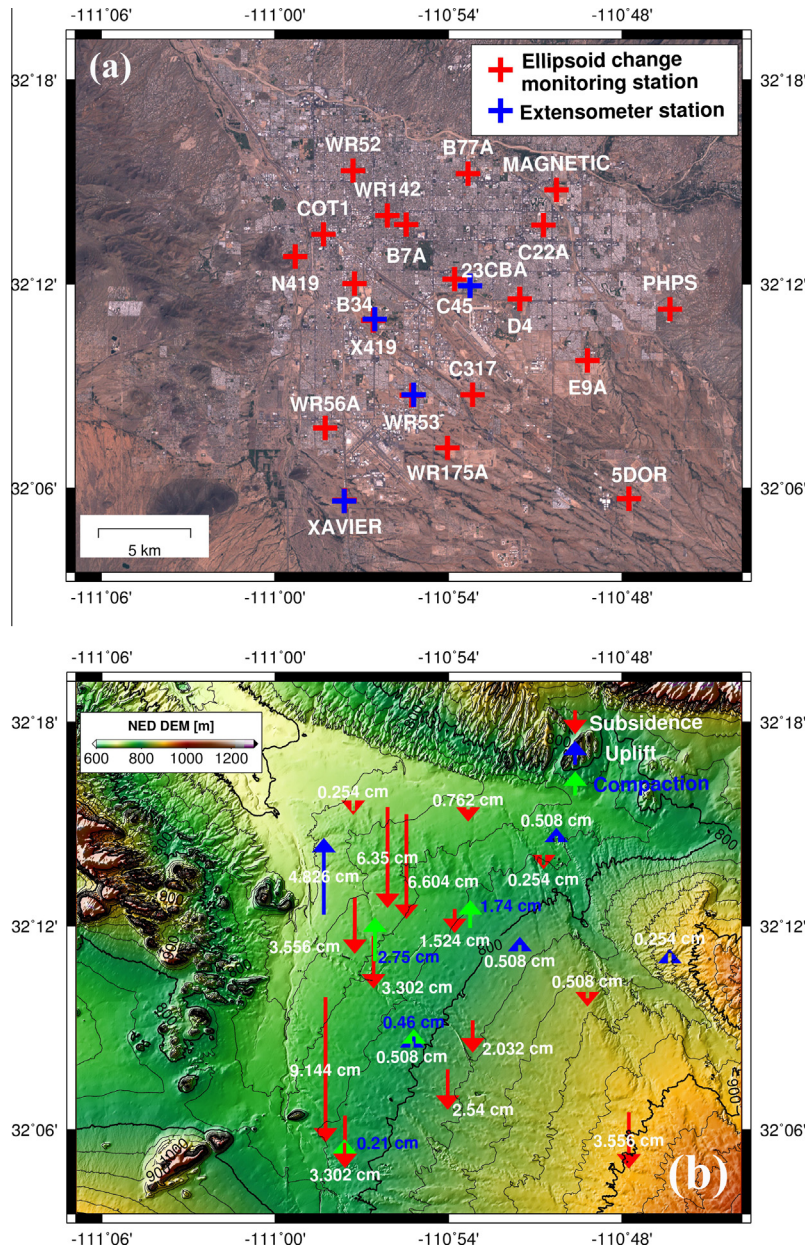


Fig. 9. (a) Land subsidence monitoring and extensometer stations installed in Tucson, and (b) Ellipsoid height changes measured in monitoring stations from 1998 to 2005; red and blue arrows represent subsidence and uplift at the sites, and the length of arrows expresses the amount of the ellipsoid height change. Green arrows represent the change of compactions, which were measured in the extensometers from October, 2005 to September, 2012. (For interpretation of the references to colour in this figure legend, the reader is referred to the web version of this article.)

processing, and simulated temporary interferogram between the gap is generated from averaging two linear deformation rates:

$$\frac{1}{2} \left(\left(\frac{\sum \phi_k^{inc}}{\sum t_k} \right)_{ERS} + \left(\frac{\sum \phi_k^{inc}}{\sum t_k} \right)_{ENVISAT} \right) \cdot (gap \text{ days/yr}) \quad (8)$$

The temporary interferogram is plotted as a dashed black line in Fig. 3(a). After SBAS processing from ERS/ENVISAT and ALOS, all outputs are filtered by Gaussian filter in time domain to suppress still-remaining atmospheric phase. Only 8 and 4 selected deformation maps are shown in Figs. 5 and 6, respectively. The selected SBAS InSAR-derived deformation maps are shown in Figs. 5–7. Forty time-series of vertical displacements corresponding to each ERS and ENVISAT acquisition date are generated (Fig. 5), and the number of C-band time-series is equal to M (number of SLC data)–1. Seven time-series of vertical displacement corresponding to

ALOS acquisition date is then created (Fig. 6). A linear deformation rate (Fig. 7) is also estimated from C-band and L-band SBAS processing. Note that the C-band deformation rate is calculated from 1993 to 2010, and the L-band deformation rate is from late 2009 to 2011. Because ALOS PALSAR data span relatively short period and their sensitivity to small deformation was low compared to C-band dataset, we did not integrate the 2 results but tried to assess them separately. Additionally, due to the same reason, we focused on analyzing C-band results more than L-band time-series products.

4. Results and discussion

The water level in the subsurface has been monitored at wells densely located in Tucson (operated by USGS Water Resources of Arizona). Because many wells were installed before 1980s, a

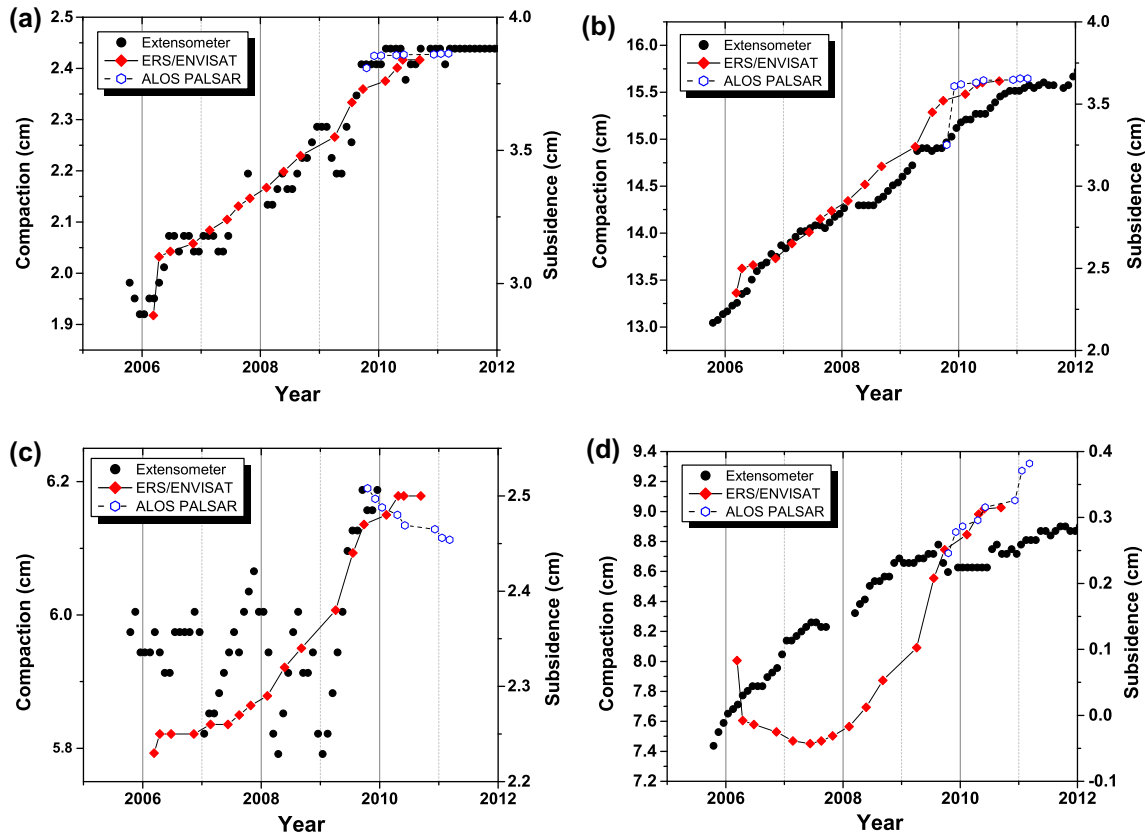


Fig. 10. Monthly compaction (blue dots) from October, 2005 to September 2012, and subsidence (red circles) estimated from ERS/ENVISAT and ALOS SBAS processing at monitoring stations of (a) WR53, (b) X419, (c) XAVIER, and (d) 23CBA. (For interpretation of the references to colour in this figure legend, the reader is referred to the web version of this article.)

long-term monitoring related to groundwater extraction has been possible (i.e. Fig. 8; 10-year interval groundwater level). The groundwater level from 1980s to 1990s (Fig. 8(a)) was dramatically dropped as much as 25 m, and the region of groundwater withdrawal was concentrated on a major residential area in Tucson. The amount of groundwater extraction was gradually reduced during 1990s (Fig. 8(b)), and the water level during 2000s (Fig. 8(c)) was recovered into a slight increase as a result of an artificial recharge into the aquifer-system. For 30 years between 1980s and 2010s (Fig. 8(d)), most of water decline occurred during the first 10 years: the maximum water decline exceeded 25 m, and most parts except the southern area had water level decrease of approximately 12 m.

The annual GPS survey campaign was conducted in multiple sites (red crosses in Fig. 9(a)), and the extensometers (blue crosses) measured the compaction of aquifer-system. The GPS-survey technique primarily estimated the vertical deformation from measured ellipsoid heights, and the increased compaction measured by extensometers implies downward land surface motion between land surface and the depth at which the bottom of the extensometer is anchored (Carruth et al., 2007). The extensometer data was acquired from USGS monitoring sites, and the annual GPS survey data is from previous USGS report (Pool and Anderson, 2008; Carruth et al., 2007). The green arrows (Fig. 9(b)) describe the compaction at the extensometer monitoring sites, and the length of arrows describes the amount of compaction from October, 2005 to September, 2012. Although there is a small number of extensometers, the region affected by large groundwater extraction indicates large compaction possibly leading to ground subsidence. The vertical deformation measured from annual GPS survey varies

among station locations, and the maximum subsidence between 1998 and 2005 reached 9.14 cm (Fig. 9(b)).

From the results of ERS/ENVISAT SBAS processing (Fig. 5), a noticeable land subsidence occurred in the center of Tucson city, around Davis Monthan Air Force Base, and near the Tucson international airport. The deformation maps show the cumulative land surface motion with respect to the acquisition date of the first SAR image (June, 22, 1993). The vertical deformation in the center of Tucson city is about 14–20 cm during 17-year period from 1993 to 2010, and the maximum subsidence of 24 cm occurred in the northern area of Tucson international airport. ALOS SBAS InSAR processing (Fig. 6) has allowed us to obtain time-series of vertical deformation from the first ALOS acquisition date (October, 17, 2009). The pattern of accumulated subsidence from ALOS InSAR pairs is different from that of ERS/ENVISAT processing due to the difference in the time-span and sensitivity to small subsidence. The linear deformation rates are calculated from the SBAS results derived from the 2 datasets separately, ERS/ENVISAT (Fig. 7(a)) indicate the maximum subsidence rate of 1.6 cm/year during 17 years, and ALOS SBAS processed results (Fig. 7(b)) delineate slowed maximum subsidence rate of 0.6 cm/year between 2009 and 2011 (Note that The PALSAR products in Figs. 6 and 7 are noisier than the ERS/ENVISAT results due to narrower color range).

When the compaction from extensometers and time-series of subsidence from SBAS processing are compared (Fig. 10), the ERS/ENVISAT and ALOS results of land subsidence from 2006 to 2011 have general agreement at stations of WR53 and X419, though both show difference between estimated deformation and compaction at XAVIER and 23CBA. When we focus on the ERS/ENVISAT SBAS InSAR-derived deformation (Fig. 10) in time-

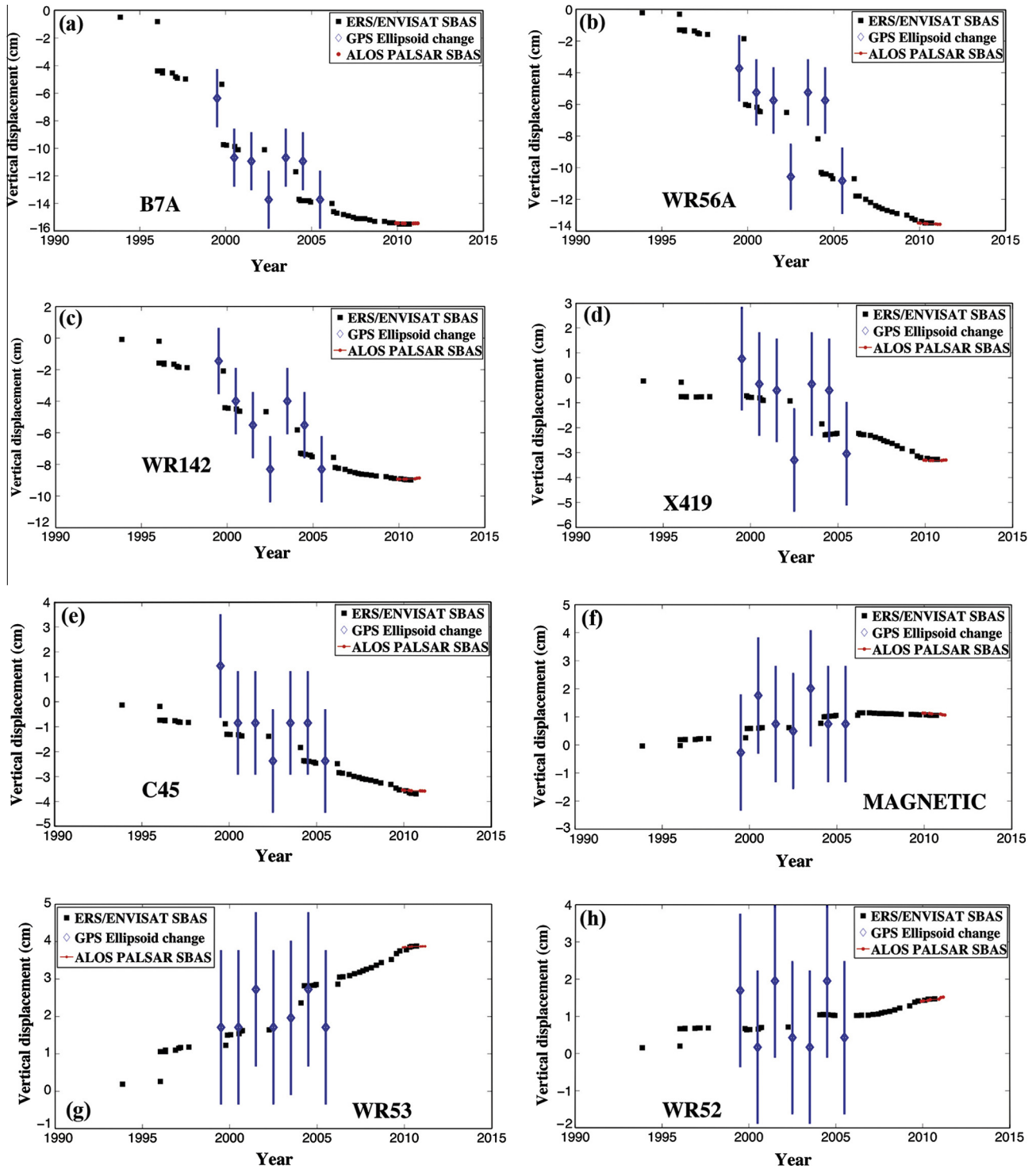


Fig. 11. Vertical displacements from ERS/ENVISAT (black squares) and ALOS (red dots) SBAS processing, and GPS ellipsoid height change (blue diamonds) from 1999 to 2005 at stations of (a) B7A, (b) WR56A, (c) WR142, (d) X419, (e) C45, (f) MAGNETIC, (g) WR53, and (h) WR52. (For interpretation of the references to colour in this figure legend, the reader is referred to the web version of this article.)

series, the subsidence in WR53 is about 0.8 cm with the compaction of 0.5 cm, and the vertical surface motion and compaction has a similar amount. Based on only the extensometer measurements, it is hard to determine the accuracy of SBAS InSAR processing (RMSE (Root Mean Square Error) 0.37 ± 0.11 cm). When considering the characteristics of the extensometers that cannot measure the subsurface change below the bottom of the device, the comparison is within a category of general agreement. The

vertical displacements from ERS/ENVISAT and ALOS SBAS InSAR processing and ellipsoid height change since 1998 (Pool and Anderson, 2008) are compared (Fig. 11). The accuracy of vertical measurement using GPS technology (error bars in Fig. 11) is assumed to be 2.032 cm (Carruth et al., 2007). In most monitoring stations, the results from GPS survey and SBAS InSAR show a similar pattern over time, and the SBAS-derived deformations are within the uncertainties of GPS measurements. Also, though

ALOS pairs span only a short time period, the results from both ERS/ENVISAT and ALOS SBAS InSAR processing are in a good agreement. In sites of B7A, WR56A, WR142, X419, and C45, both of GPS and SBAS InSAR-derived deformation describes the ground subsidence due to the groundwater extraction. However, in some places of MAGNETIC, WR53, and WR52, the ground was in uplift and it could be attributed to rebounding of ground surface after groundwater recovery.

The temporal groundwater elevation measured at wells was also compared with ERS/ENVISAT SBAS-processed vertical displacement (Fig. 12). The pattern of groundwater elevation change was observed in most wells of Tucson. The groundwater level was declining until 2003, and an artificial recharge and reduced consumption of groundwater brought out the recent increase of water table. At station WR56A, the ground subsidence was about 15 cm during observation period. The surface is still subsiding after 2003 despite less rapidly. The continuous subsidence implies that the subsidence could be affected by delayed compaction and inelastic behavior, while the deformation is not recovered but permanent. In WR52, the land surface with increased groundwater level is in uplift. It indicates that the displacement in the location is elastic, while the increase of groundwater caused a recovery of subsurface.

The contour deformation map (Fig. 13(a)) delineates several major subsidized regions affected by groundwater extraction. A, B, and D regions are near the center of Tucson city, C is close to Davis Monthan Air Force Base, and E region is around the northern part in Tucson International Airport. A and B regions have the subsidence of about 14 cm, and C and D areas are affected by 4 cm subsidence. E regions have the maximum subsidence exceeding 20 cm during 17-year span. When comparing the contours of water level changes and linear deformation map (Fig. 7), and the subsidence map (Fig. 14(a)), A and B regions are close to the areas of maximum water level changes (up to 24 m) since 1980s. C and D areas are overlapped with a region of relatively small water level change (up to 10 m). Because the change of groundwater and surface motion is correlated, the result explains that the groundwater level change caused the ground deformation in A, B, C, and D. On the other hand, other areas with large water level change do not have a significant subsidence. The reasonable assumption is that clay thickness is not sufficient for sensitive response to the change of aquifer-system in the subsurface, or a soil layer is over-consolidated and incompressible and the surface

is very stabilized. E region with maximum subsidence is another exception, because the groundwater level change is not highly correlated with subsidence. The E region in Figs. 8(d) and 9(b) is in the mix of increase and decrease of groundwater level, and the change of aquifer-system may not be a major cause of large subsidence. Possibly, the human construction of roads, buildings, and airport can cause a large vertical deformation in E region, but, currently, it is not clear which factors mostly affected the vertical deformation in E area.

One of great advantages of SBAS InSAR processing is that it could estimate vertical deformation between two particular acquisition dates. The difference of cumulative deformations of two particular dates can delineate temporal evolution of subsidized areas in Tucson. Images in Fig. 13(b)–(g) are generated from the difference of deformation maps (Fig. 5) with about three-year interval, estimated from ERS/ENVISAT SBAS InSAR processing. Red-colored regions in Fig. 13(b)–(g) mean ground subsidence, and dark red color is approximated as maximum subsidence. Between 1996 and 1999, B and E region shows maximum subsidence exceeding 1.6 cm. During the span of 1999 and 2002, the maximum subsidence (dark red) of B and E embraces the largest area in Tucson. Between 2004 and 2007 (Fig. 13(f)), the subsidence rate of A and B is slowed down, but the C region has enlarged subsidence area since 1999. The recent observation (Fig. 13(g)) indicates a slowing subsidence in most regions of Tucson. The subsidence in A region is almost disappeared, and B region shows only a small subsidence less than 1 cm. The C region near Davis Monthan Air Force Base shows still growing subsidized region from 1999 to 2010. The subsidence area in E region between 2007 and 2010 is much smaller than the areas during other periods. Due to the similar time span, the Fig. 13(g) is well fitted to the result from ALOS SBAS InSAR processing in Fig. 7(b), characterizing a major subsidence in B, C, and E region. The profile along the lines of a–a', b–b', c–c', and d–d' in Fig. 13(c) characterizes the features of slowing-down subsidence in Tucson (Fig. 14). The B and E region shows the most prominent subsidence (~5 cm) of 3-year interval from 1993 to 2010. In most regions, the subsidence between 1996 and 1999 is most significant and the displacement from 2007 to 2010 is less than that from other 3-year periods. However, the subsidence of C region was recently developed between 2007 and 2010 in contrary to other regions. The images in Fig. 14 attest that the subsidence in most areas is gradually slowing down due to the recharge of groundwater.

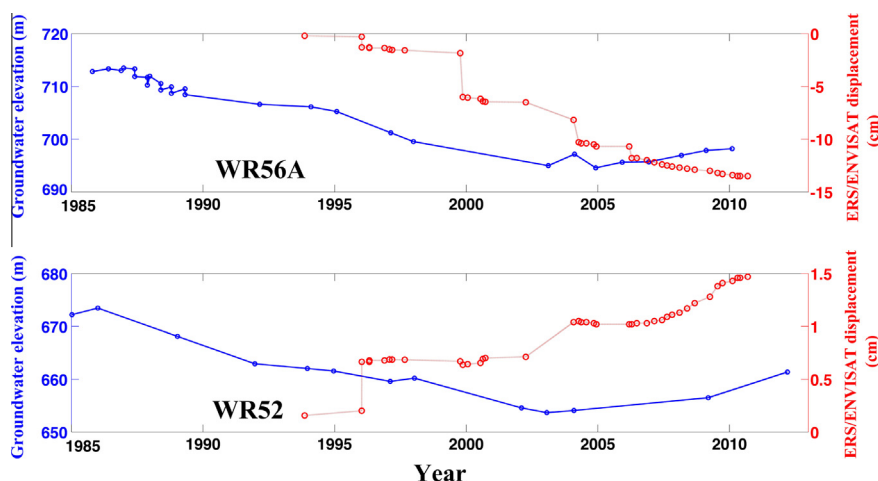


Fig. 12. Time-series vertical deformation (red circles and lines) from ERS/ENVISAT SBAS processing and groundwater elevation (blue dots and lines) measured in WR56A and WR52. (For interpretation of the references to colour in this figure legend, the reader is referred to the web version of this article.)

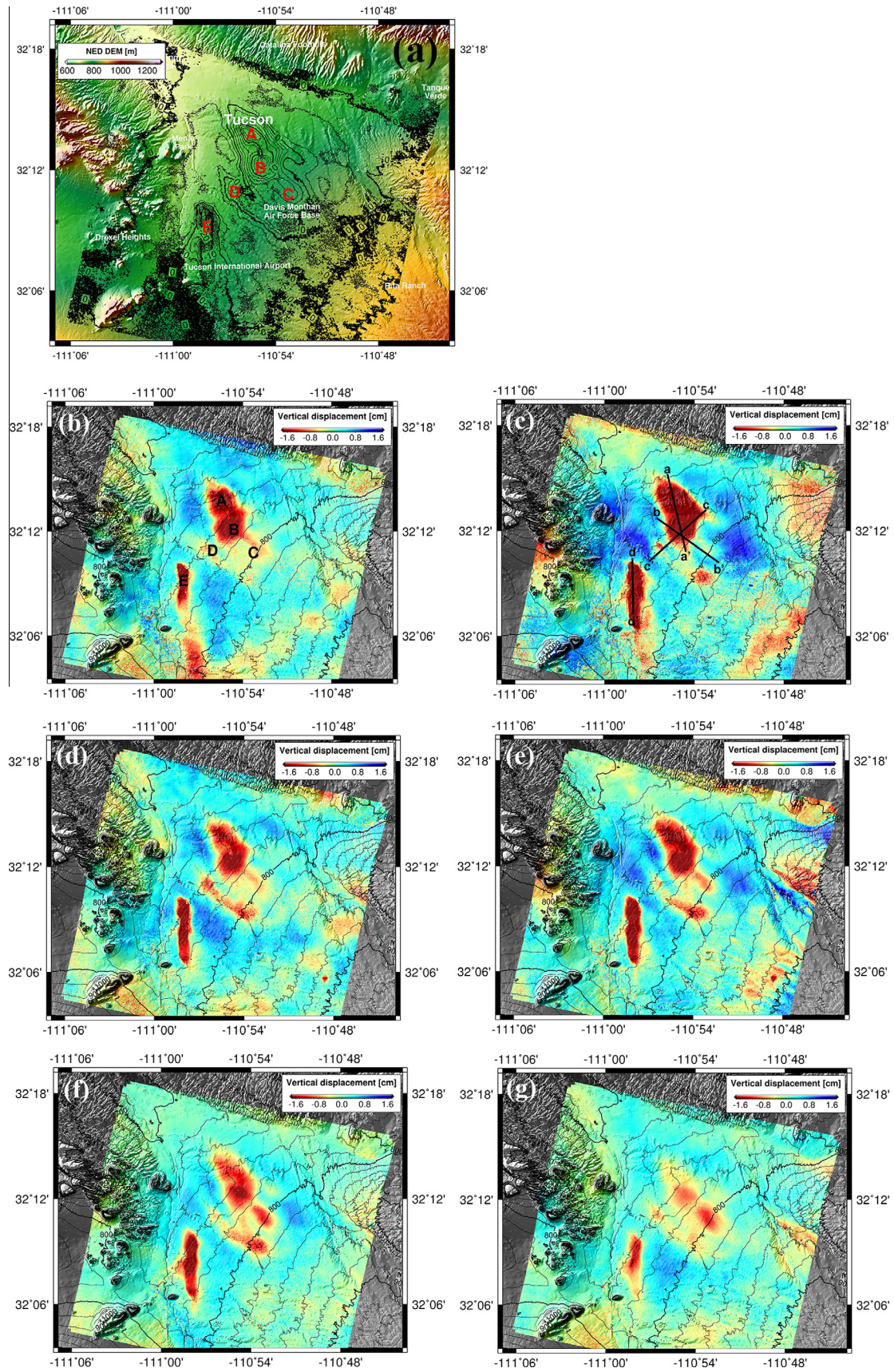


Fig. 13. (a) Contour in a plain view of ERS/ENVISAT SBAS InSAR-derived vertical deformation during 17-year span (A, B, C, D, and E regions are mostly affected by ground subsidence), and 3-year interval ERS/ENVISAT SBAS InSAR-derived vertical deformation of (b) 1993.11.09–1996.11.22, (c) 1996.11.22–1999.11.12, (d) 1999.11.12–2002.04.05, (e) 2002.04.05–2004.12.10, (f) 2004.12.10–2007.10.26, and (g) 2007.10.26–2010.09.10.

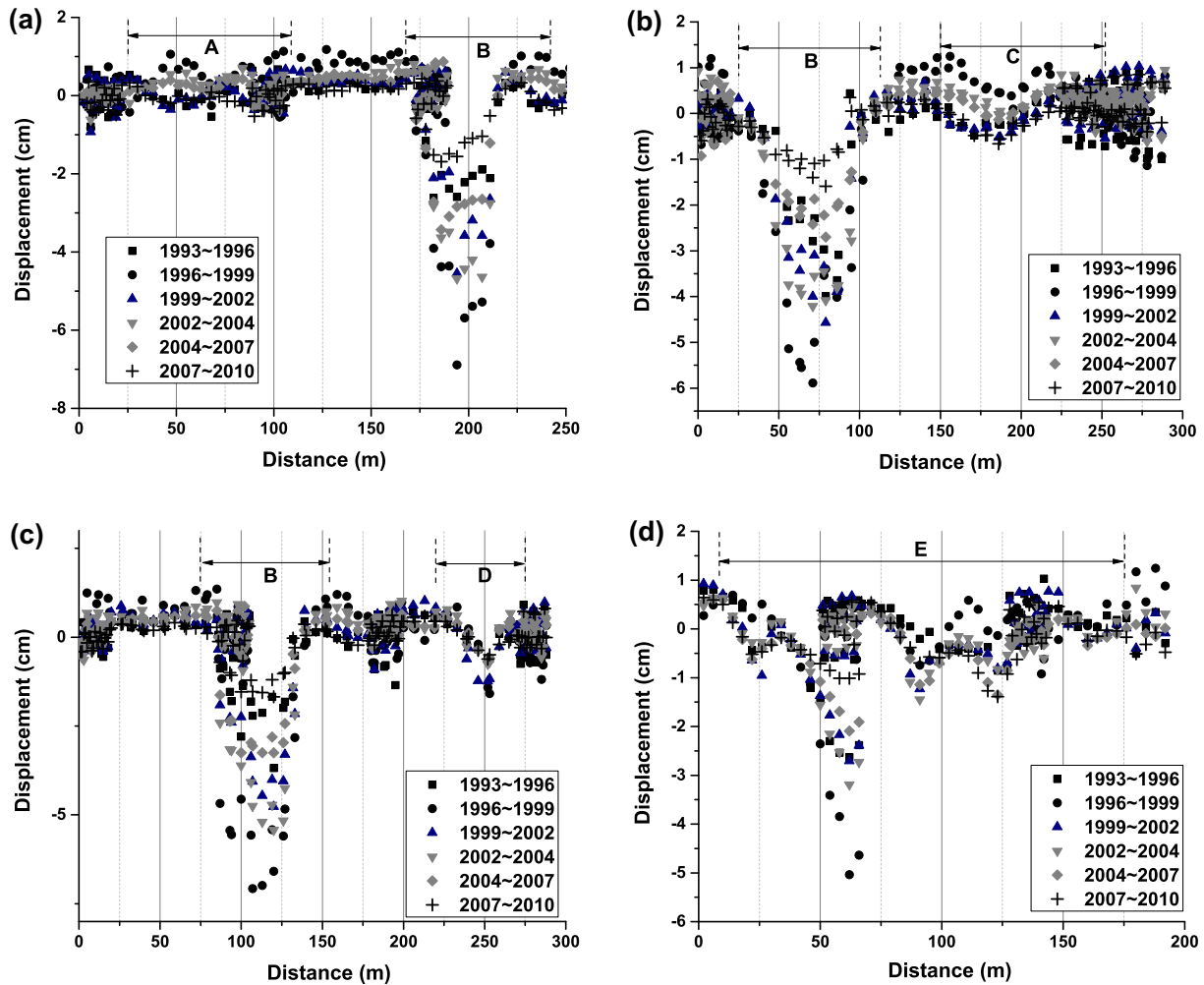


Fig. 14. 3-year interval vertical displacements along the profiles of (a) a–a', (b) b–b', (c) c–c', and (d) d–d' in Fig. 13(c).

5. Conclusion

Our multi-sensor SBAS InSAR processing delineated a long-term development of the vertical deformation from 1993 to 2011, though ALOS InSAR pairs covered a relatively short time period between late 2009 and 2011. Most analyses focused on products from ERS/ENVISAT SBAS processing due to a longer time-span and high sensitivity to small and slow-developing subsidence. Although there is no a “real” ground-truth reference in our interest area, the compaction from extensometer the ellipsoid height changes measured by the annual GPS survey show a similar pattern with land subsidence estimated from SBAS processing in spite of differences in certain stations. The 3-year interval maps of vertical deformation reveal the characteristics of subsidence, which had occurred in Tucson. The subsidence during mid- and late-1990s was significant around the large groundwater-withdrawal areas, but our results imply that the recent subsidence in most areas of Tucson is slowing down and is about to cease, based on the estimation between 2007 and 2010. The halting subsidence is attributed to an intense effort to conserve groundwater, because Tucson is recharging groundwater supplies by running part of its share of Central Arizona Project (CAP) water into various open portions of local rivers to seep into their aquifer (Pool and Anderson, 2008). However, the human activities and still-progressing groundwater extraction can be critical for the turn-around of current ceasing subsidence and future development of deformation.

Our study has demonstrated that the SBAS InSAR processing is valuable for estimating slow subsidence caused by spatio-temporal responses of aquifer system. However, in this study, we assumed that groundwater withdrawal is the most dominant factor in the subsidence of Tucson. Moreover, the human activities (i.e. constructing buildings and airports) except groundwater use and other natural factors were not elaborately considered, but the future study should focus on unraveling more parameters, which are related with ground motions. Additionally, the future dense temporal and high-resolution SAR observations from Sentinel-1, TerraSAR-X, and ALOS-2 PALSAR-2 will help to obtain more precise measurements and find more robust relationship among ground deformation in Tucson, groundwater extraction, and other parameters.

Acknowledgements

This research was supported by grants from the Shuler-Foscue Endowment at Southern Methodist University and NASA's Earth Surface & Interior Program (NNX14AD95G), United States Geological Survey (G12AC20468), NASA Earth and Space Science Fellowship program (NNX10AN54H) and Geodetic Imagery Program (NNX12AQ07G), and the Chinese Academy of Sciences/SAFEA International Partnership Program for Creative Research Teams (KZZD-EW-TZ-05). The SAR data used in the study were provided by ESA (ENVISAT ASAR) and JAXA (ALOS PALSAR) via

approved data proposals. The InSAR results were generated by GAMMA software, and most figures were created by GMT (Generic Mapping Tools).

References

- Amelung, F., Galloway, D.L., Bell, J.W., Zebker, H., 1999. Sensing the ups and downs of Las Vegas: InSAR reveals structural control of land subsidence and aquifer-system deformation. *Geology* 27 (6), 483–486.
- Bell, J.W., Amelung, F., Ramelli, A.R., Blewitt, G., 2002. Land subsidence in Las Vegas, Nevada, 1935–2000: new geodetic data show evolution, revised spatial patterns, and reduced rates. *Environ. Eng. Geosci.* 8 (3), 155–174.
- Berardino, P., Fornaro, G., Lanari, R., Sansosti, E., 2002. A new algorithm for surface deformation monitoring based on small baseline differential SAR interferograms. *IEEE Trans. Geosci. Remote Sens.* 40 (11), 2375–2383.
- Carruth, R.L., Pool, D.R., Anderson, C.E., 2007. Land subsidence and aquifer-system compaction in the Tucson Active Management Area, south-central Arizona, 1987–2005. U.S. Geological Survey Scientific Investigations Report 2007-5190, 27 p.
- Galloway, D.L., Hoffmann, J., 2007. The application of satellite differential SAR interferometry-derived ground displacements in hydrogeology. *Hydrogeol. J.* 15 (1). <http://dx.doi.org/10.1007/s10040-006-0121-5>, 133–154.
- Galloway, D.L., Hudnut, K.W., Ingebritsen, S.E., Phillips, S.P., Peltzer, G., Rogez, F., Rosen, P.A., 1998. Detection of aquifer-system compaction and land subsidence using interferometric synthetic aperture radar, Antelope Valley, Mojave Desert, California. *Water Resour. Res.* 34, 2573–2585.
- Galloway, D.L., Jones, D.R., Ingebritsen, S.E., 2000. Measuring Land Subsidence from Space. U.S. Geological Fact Sheet 051-00, 4 p.
- Hanssen, R.F., 2001. *Radar Interferometry: Data Interpretation and Error Analysis*. Kluwer Academic Publishers.
- Hoffmann, J., Zebker, H.A., 2003. Prospecting for horizontal surface displacements in Antelope Valley, California, using satellite radar interferometry. *J. Geophys. Res.* 108 (F1), 6011, <http://dx.doi.org/10.1029/2003JF000055>.
- Lanari, R., Mora, O., Manunta, M., Mallorquí, J.J., Berardino, P., Sansosti, E., 2004. A small-baseline approach for investigating deformations on full-resolution differential SAR interferograms. *IEEE Trans. Geosci. Remote Sens.* 42 (7), 1377–1386.
- López-Quiroz, P., Doin, M.-P., Tupin, F., Briole, P., Nicolas, J.-M., 2009. Time series analysis of Mexico City subsidence constrained by radar interferometry. *J. Appl. Geophys.* 69, 1–15.
- Lu, Z., 2007. InSAR imaging of volcanic deformation over cloud-prone areas – Aleutian Islands. *Photogramm. Eng. Remote Sens.* 73, 245–257.
- Lu, Z., Danskin, W., 2001. InSAR analysis of natural recharge to define structure of a ground-water basin, San Bernardino, California. *Geophys. Res. Lett.* 28, 2661–2664.
- Luo, Q., Perissin, D., Zhang, Y., Jia, Y., 2014. L- and X-band multi-temporal InSAR analysis of Tianjin subsidence. *Remote Sens.* 6, 7933–7951.
- Pepe, A., Sansosti, E., Berardino, P., Lanari, R., 2005. On the generation of ERS/ENVISAT DInSAR time-series via the SBAS technique. *IEEE Geosci. Remote Sens. Lett.* 2 (3), 265–269.
- Pool, D.R., 2005. Variations in climate and ephemeral channel recharge in southeastern Arizona, United States. *Water Resour. Res.* 41, W11403. <http://dx.doi.org/10.1029/2004WR003255>, 24 p.
- Pool, D.R., Anderson, M.T., 2008. Ground-water storage change and land subsidence in Tucson Basin and Avra Valley, southeastern Arizona, 1998–2002. U.S. Geological Survey Scientific Investigations Report 2007-5275, 34 p.
- Samsonov, S., 2010. Topographic correction for ALOS PALSAR interferometry. *IEEE Trans. Geosci. Remote Sens.* 48 (7), 3020–3027.
- Samsonov, S., d'Oreye, N., 2012. Multidimensional time series analysis of ground deformation from multiple InSAR data sets applied to Virunga Volcanic Province. *Geophys. J. Int.* 191 (3), 1095–1108.
- Samsonov, S., Beavan, J., Gonzalez, P., Tiampo, K.J.F., 2011. Ground deformation in the Taupo Volcanic Zone, New Zealand observed by ALOS PALSAR interferometry. *Geophys. J. Int.* 187 (1), 147–160.
- Samsonov, S., d'Oreye, N., Smets, B., 2013. Ground deformation associated with post-mining activity at the French–German border revealed by novel InSAR time series method. *Int. J. Appl. Earth Obs. Geoinf.* 23, 142–154.
- Sandwell, D.T., Myer, D., Mellors, R., Shimada, M., Brooks, B., Foster, J., 2008. Accuracy and resolution of ALOS interferometry: vector deformation maps of the father's day intrusion at Kilauea. *IEEE Trans. Geosci. Remote Sens.* 46 (11), 3524–3534.
- Schmidt, D.A., Bürgmann, R., 2003. Time-dependent land uplift and subsidence in the Santa Clara valley, California, from a large interferometric synthetic aperture radar data set. *J. Geophys. Res.* 108 (B9), 2416. <http://dx.doi.org/10.1029/2002JB002267>.
- Tikhonov, A.N., Arsenin, V.Y., 1977. *Solution of Ill-Posed Problems*. V. H. Winston and Sons, Washington, DC.
- Tong, X., Sandwell, D.T., Fialko, Y., 2010. Coseismic slip model of the 2008 Wenchuan earthquake derived from joint inversion of interferometric synthetic aperture radar, GPS, and field data. *J. Geophys. Res.* 115, B04314. <http://dx.doi.org/10.1029/2009JB006625>.